Solar Physics (2025) 300:29
https://doi.org/10.1007/s11207-025-02437-9

RESEARCH

Mysteries of the 17 May 2012 Solar Event Responsible for GLE71: II. Features of the Flare and Its Atypical Microwave Emission

V.V. Grechnev[1] · **V.I. Kiselev**[1] · **A.M. Uralov**[1] · **N.S. Meshalkina**[1] ·
A.L. Lysenko[2]

Received: 9 November 2024 / Accepted: 7 February 2025

Abstract
As known, large near-Earth proton enhancements usually occur after major eruptive solar flares accompanied by strong microwave bursts. Typically, the spectral-maximum frequency of such a burst exceeds 10 GHz, and the flux exceeds 10^4 sfu. Ground-level cosmic-ray enhancements (GLEs) are the most energetic subset of large proton events, and it seems that microwave bursts in GLE-associated flares should follow this pattern. This is true in most cases, but in individual events that have produced GLEs, only moderate microwave bursts have been observed. In particular, in the SOL2012-05-17 event responsible for GLE71, the spectral-maximum frequency of the microwave burst did not exceed 10 GHz, and the flux did not reach 10^3 sfu. We found that the temporal profile of the microwave burst followed the smoothed magnetic-reconnection rate, lagging behind it by about 50 s and that the burst properties were determined by the following circumstances: i) the magnetic configuration was asymmetric, and ii) the sources of the gyrosynchrotron emission were the entire flare arcade and a compact region above the sunspot umbra. Observations directly demonstrated these features, which were previously inferred for the SOL2001-12-26 event responsible for GLE63. A long-known discrepancy was observed between the estimates of the electron spectrum obtained from hard X-rays and microwaves. However, the hardening of the spectrum of trapped electrons that has been invoked to explain this discrepancy was not found in this event. Indications of a relationship between flare processes and proton acceleration are discussed.

Keywords Energetic particles · Flares · Magnetic fields · Magnetic reconnection · Radio bursts · X-ray bursts

1. Introduction

Solar eruptions and flares are potential sources of space-weather disturbances that can disrupt both ground-based and space-borne systems. Some disturbances even pose a radiation hazard to those people who are not protected by the full thickness of the Earth's atmosphere. The sources of some space-weather disturbances have been identified, e.g., coronal

---

Extended author information available on the last page of the article mass ejections (CMEs) whose magnetic fields cause geomagnetic storms, or ionizing radiation from flares that causes radio blackouts. The sources of some other disturbances remain unclear.

Perhaps the most controversial is the origin of solar energetic protons, which make up a significant part of solar energetic particles (SEPs). Fluxes of solar and secondary particles pose a hazard to passengers and crew on aircraft flying at high latitudes, as well as to astronauts on spacecraft, who may be exposed to significant radiation doses. To prevent this, transcontinental flight routes were changed when solar activity increased remarkably in late October 2003 (Veselovsky et al. 2004). Occasionally, the energy of solar protons is so high that secondary neutrons produced by their collisions with nuclei in the Earth's atmosphere reach the ground. Since 1942, only 76 such ground-level enhancements (GLEs) of cosmic-ray intensity have been recorded (Miroshnichenko, Vashenyuk, and Pérez-Peraza 2013; Anastasiadis et al. 2019). The 17 May 2012 event produced GLE71 (e.g. Gopalswamy et al. 2013b; Mishev, Kocharov, and Usoskin 2014).

So far, there is no consensus on where, when, and under what conditions solar protons are accelerated. There are two possible accelerators of charged particles: i) flare processes in active regions caused by magnetic reconnection and ii) shock waves excited by eruptions. Flare processes occur in hot regions in the lower corona, whereas shock acceleration occurs in the outer corona at lower temperatures. Based on these ideas, efforts have been made to identify the sources of solar accelerated protons from indirect indications inferred from observations.

Several decades ago, it was noted that large near-Earth proton enhancements occur after prolonged flares that are accompanied by strong microwave bursts (e.g. Croom 1971; Castelli and Barron 1977; Akinian et al. 1978). This pattern and its subsequent studies provided the basis for dividing solar events into impulsive, electron-rich, and gradual, proton-rich events. The idea of different acceleration mechanisms in these two categories of events emerged. The correlation of proton increases with microwave bursts suggested the simultaneous acceleration of electrons and protons by flare processes. Observations of nuclear γ-ray emission and radio bursts (e.g. Hirasima, Okudaira, and Yamagami 1970; Forrest and Chupp 1983; Forrest et al. 1986) supported such views.

The flare origin of solar protons has been challenged by Kahler (1982), who argued that only CME-driven shocks accelerate them. He proposed that the correlation between microwave bursts and proton enhancements was due to a general correspondence between the energy release in a big eruptive flare and its various manifestations. Thus, it was to be expected that this "big flare syndrome" should lead to a correlation between the various parameters, regardless of any physical connection between them. The results of several subsequent studies of near-Earth proton enhancements appeared consistent with this idea. Indeed, several properties of the SEP composition indicated their shock-related origin in the lower-temperature corona rather than in a hot flare region. These are, for example, the Fe/O, ^{3}He/^{4}He, and H/He ratios, the iron charge state, and some other properties (e.g. Tylka et al. 2005; Reames 2013).

A well-developed scenario for SEP acceleration by a CME-driven shock assumes that the bow shock begins to form when the nose of the outer surface of the CME exceeds the Alfvén speed in the environment. This view leads to the following concept (e.g. Reames 2009, 2013): the shock is thought to form at a considerable height, well after the impulsive phase of the flare. The onset of a type II burst is thought to mark the appearance of the shock (e.g. Gopalswamy et al. 2013a). The release of shock-accelerated protons into interplanetary space is expected from this moment onwards. The appearance of flare-accelerated protons is assumed to be possible during the impulsive phase, but their release is prevented by the closed flare magnetic configuration. Consistent with these expectations, the release times of protons and heavier ions, estimated from velocity-dispersion analysis for a number of events by Reames (2009) and in other studies, were found to be after the impulsive phase of the flares. Perhaps all these circumstances have reduced interest in flares in the context of SEP protons.

However, some findings in recent decades do not seem to be in agreement with this scenario. These results affect the relative timing of the release of accelerated protons and the shock-wave excitation with respect to the impulsive phase.

In the model proposed by Masson, Antiochos, and DeVore (2013), flare-accelerated particles are injected both downward into the flare loops, where electrons produce hard X-rays (HXR) and microwaves, and upward into the forming magnetic flux rope (e.g. Longcope and Beveridge 2007). The electrons and protons then remain trapped in the expanding flux rope until it reconnects with an open magnetic structure, when they escape into interplanetary space. Thus the release of flare-accelerated particles appears to occur after the impulsive phase. This scenario was supported by Kocharov et al. (2017) and Grechnev et al. (2017b). It was found that the particle-release times estimated by Reames (2009) for most of the events he examined were close to the onset times of decametric type IIIs, which indicated the escape of accelerated electrons.

Further, a number of studies, both ours (e.g. Grechnev et al. 2011, 2016, 2017b, 2024) and those of other authors (e.g. Bain et al. 2012; Zimovets et al. 2012), concluded that a shock wave initially arises during the impulsive phase of the flare as a piston shock, then turns into a blast wave, and only after that becomes a bow shock if the CME behind it is fast. Hence, shock-accelerated protons may hypothetically appear even earlier than those flare-accelerated. Another conclusion is that a type II burst starts when the flank or front of a shock wave traveling through the corona encounters a streamer. Wave energy accumulates near the current sheet in the streamer, causing a flare-like process to run along the streamer, producing narrow-band harmonic type II radio emission. These conclusions change the meaning of the results of the velocity-dispersion analysis to the opposite. Thus at least some of the criteria that have previously been attempted to identify SEP proton sources do not actually allow this to be done. Careful selection of some other criteria is required to take into account the recently revealed circumstances mentioned. In the meantime, there seems to be no compelling reason to disregard either of the possible sources of SEP protons.

In the twenty-first century, localization of solar γ-ray emission centroid position became possible (without resolving the source structure). In 2002 – 2003 the Reuven Ramaty High-Energy Solar Spectroscopic Imager (RHESSI: Lin et al. 2002) allowed the localization of the 2.223 MeV neutron-capture line sources in several events (Hurford et al. 2003, 2006). They were located in flare regions, although they did not always coincide with HXR sources (Vilmer, MacKinnon, and Hurford 2011). Since 2008, observations by the Fermi Large Area Telescope (LAT: Atwood et al. 2009) have made it possible to localize sources of high-energy γ-ray emission. The centroid positions of the > 100 MeV emission, which is due to the decay of pions produced by > 300 MeV protons, are close to the flare sites for almost all events listed in the LAT catalog (Ajello et al. 2021).

Thus some manifestations indicate one origin of energetic protons, whereas others indicate another. This duality suggests contributions from both flare processes and shock waves to proton acceleration. Klein and Trottet (2001) proposed that shock acceleration dominates at lower proton energies, whereas flare acceleration dominates at high energies. Statistical studies by Dierckxsens et al. (2015), Trottet et al. (2015), Papaioannou et al. (2016), and Kiselev, Meshalkina, and Grechnev (2022) indeed support this idea. Thus the existence of a relationship between flare manifestations such as microwave bursts, on the one hand, and near-Earth proton enhancements, on the other hand, must have more substantial causes than the indirect correlation due to the "big flare syndrome" and deserve attention.

Statistical studies by Grechnev et al. (2013b, 2015) revealed a weak, scattered relationship between the peak fluxes of 35 GHz bursts and the peak fluxes of near-Earth protons with energies > 100 MeV and a higher correlation between their fluences (time-integrated fluxes). It was also found that a large proton event typically occurs if the microwave burst has a spectral-maximum frequency > 10 GHz and the peak flux of this burst exceeds 10^4 sfu. Besides events following this pattern, a few events were identified whose proton yield was much higher, whereas the microwave burst was moderate. Two of these events were associated with GLEs, SOL2001-12-26 (GLE63) and SOL2012-05-17 (GLE71). Analyzing the former flare, Grechnev et al. (2017a) inferred that the reasons for its peculiarities were: i) an asymmetric magnetic configuration and ii) the fact that the gyrosynchrotron emission was produced by accelerated electrons in the entire multiloop arcade.

The latter conclusion seems consistent with the two-dimensional CSHKP flare model (Carmichael 1964; Sturrock 1966; Hirayama 1974; Kopp and Pneuman 1976; for a review see also, e.g., McKenzie 2002) and its three-dimensional (3D) extensions (e.g. Longcope and Beveridge 2007; Aulanier, Janvier, and Schmieder 2012). However, only a few compact nonthermal sources almost always appear in HXR and microwaves. Such morphologies observed in impulsive flares suggest that only a pair of loops are involved in nonthermal processes (Hanaoka 1997; Nishio et al. 1997). The idea of such configurations was then extended to some long-duration flares (e.g. Tzatzakis, Nindos, and Alissandrakis 2008). As a result, researchers have focused on individual flare loops (e.g. Simões and Costa 2010; Costa et al. 2013; Motorina, Fleishman, and Kontar 2020).

As our analysis of the 17 May 2012 event in Grechnev et al. (2024) (hereafter Article I) stated, neither of the possible sources of protons, i.e., the shock wave and the flare, has been sufficiently studied. The traditional idea of the initial bow-shock excitation, on which the considerations of Gopalswamy et al. (2013b), Shen et al. (2013), and Rouillard et al. (2016) were based, has not been confirmed. Article I found that the event involved two eruptions, whereas the shock-wave history was more complex than these studies assumed. As for the flare, we are only aware of the study by Firoz et al. (2017) of its late-stage thermal emission.

In this article we analyze the features of the 17 May 2012 flare and its microwave emission. Their similarity to the mentioned 26 December 2001 flare allows us to verify the conclusions drawn from the analysis of that flare. The question arises as to what was specific to these two flares and what was typical. There remain issues not addressed previously, such as the relationship of microwave emission with magnetic reconnection and with HXR emission. A more complete knowledge of the features of the shock wave and the flare in this event responsible for GLE71 will help to find suitable criteria for identifying SEP proton sources.

This article is organized as follows. Section 2 addresses the flare configuration. Section 3 considers the temporal course of the flare. Section 4 addresses the structure of microwave sources. Section 5 analyzes HXR and microwave spectra. Section 6 discusses the results and their implications.

2. Flare Morphology and Magnetic Configuration

The 17 May 2012 flare occurred in active region (AR) 11476 that had a $\beta\gamma\delta$ magnetic configuration. According to observations of the Geostationary Operating Environmental Satellites (GOES), the flare started at 01:25 UT, reached maximum at 01:47 UT, and ended at

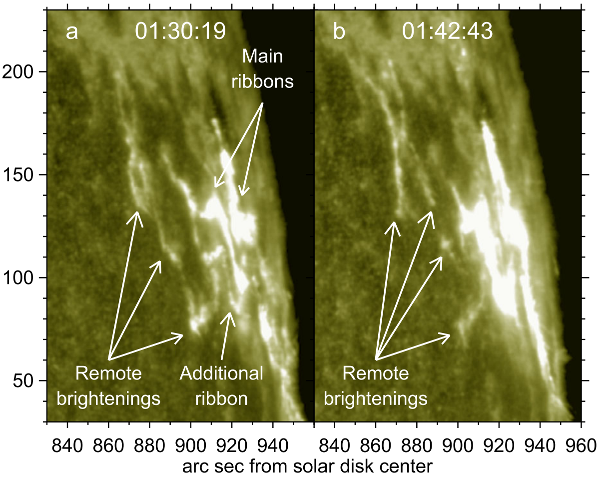

Figure 1 Main flare ribbons, an additional ribbon parallel to the eastern main ribbon, and remote elongated brightenings visible in AIA 1600 Å images. To reveal weak remote brightenings, the brightness of the main ribbons is limited from above, distorting their appearance.

02:14 UT. The GOES importance of this M5.1 flare was the lowest among not occulted GLE-related flares in four decades (see Cliver 2006) and comparable to the mentioned 26 December 2001 M7.1 flare associated with GLE63. The reported flare location was N11 W76. The eruptive flare was observed in ultraviolet (UV) and the extreme ultraviolet (EUV) by the Atmospheric Imaging Assembly (AIA: Lemen et al. 2012) on board the Solar Dynamics Observatory (SDO: Pesnell, Thompson, and Chamberlin 2012).

Article I addressed the eruptions, refined the position of the main flare site to N06 W78, and established that this was a two-ribbon flare complicated by the presence of additional ribbons. The SDO/AIA 1600 Å images in Figure 1 show the flare structures and their changes from the onset of the impulsive phase in Figure 1a to the maximum of the last flare peak in Figure 1b. The additional ribbons, one of which is visible in Figure 1a, were located almost parallel to the main ribbons. The presence of these additional ribbons is caused by two eruptions that occurred shortly after each other. In addition, weak remote ribbon-like structures were observed. Comparison of their north-eastern parts in Figures 1a and 1b shows their change during the impulsive phase.

Article I demonstrated the expected correspondence between the reconnection rate and the HXR burst. In this article we aim to reveal the features of this correspondence in microwave emission. The reconnected magnetic flux is generally found by calculating the total positive and total negative magnetic fluxes within the cumulative area covered by the flare ribbons at the current time. Then, differentiation of the cumulative magnetic flux provides the magnetic-flux change rate. To calculate the reconnected magnetic flux, we used the radial magnetic component computed from the full-disk vector magnetic-field data routinely provided by the Helioseismic and Magnetic Imager (HMI: Scherrer et al. 2012) on board SDO. We also use the radial magnetic-field distribution in the analysis of the flare configuration, since line-of-sight (LOS) magnetograms are strongly distorted near the limb.

In our calculations, we followed the approach developed by Harvey (1969), as described in Article I. The input full magnetic-field vector data were taken from the `hmi.B_720s` series files accessible at the Joint Science Operations Center (JSOC). The `disambig` file contains the information about the resolved 180°-ambiguity of the transverse magnetic component (see also Sun 2013, for more details). To avoid possible distortions caused by flare emission, we used the vector magnetogram observed shortly before the flare and then transformed the resulting radial magnetogram to the time point of interest.

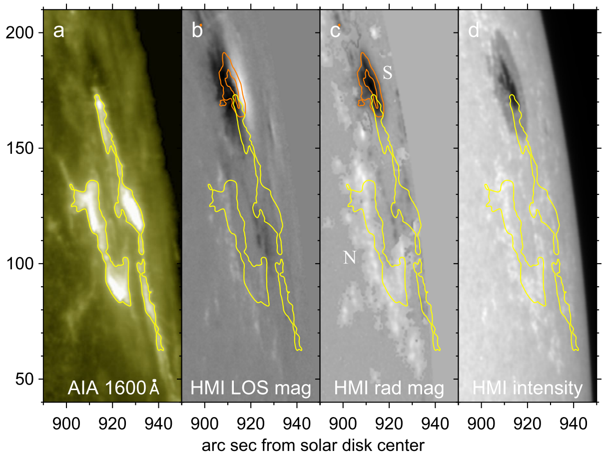

Figure 2 Main flare ribbons (*yellow contours*, same in all panels) in AIA 1600 Å image (**a**) compared to line-of-sight magnetogram (**b**), radial magnetic-field distribution (**c**), and intensitygram (**d**). The levels of *red contours* in panels b and c are [−1000, −2000] G. Labels *N* and *S* in panel c indicate magnetic polarities. All images refer to 01:42:43 UT.

Figure 2a shows the same SDO/AIA 1600 Å image as in Figure 1b. The yellow contours of the main flare ribbons found from this image are overlaid on the LOS magnetogram in Figure 2b, radial magnetogram in Figure 2c, and intensitygram in Figure 2d, all of which are based on SDO/HMI data. Comparison of these images reveals distortions in the LOS magnetogram and provides insight into the actual magnetic configuration.

The polarities of the eastern parts of the magnetic structures visible on the radial magnetogram in Figure 2c coincide with their counterparts in the LOS magnetogram in Figure 2b. The western parts of these structures appear in reverse polarity, as is usually observed near the limb. The radial magnetogram shows a simpler magnetic-field distribution compared to the LOS magnetogram and appears to match the intensitygram in Figure 2d better.

A sunspot resided at the northern edge of the flaring active region. The western part of the sunspot in the LOS magnetogram (Figure 2b) had a spurious positive (N) polarity, whereas the entire sunspot in the radial magnetogram (Figure 2c) had negative (S) polarity. The red contours correspond to the [−1000, −2000] G levels in the radial magnetogram. Magnetic fields outside the sunspot were considerably weaker. The eastern flare ribbon was located in the N-polarity. The western ribbon was in the S-polarity and entered the strongest magnetic fields above the sunspot umbra. Note that the contour of the western ribbon has not caught the weaker northernmost brightening in the sunspot; hence the flare process actually penetrated even deeper into the region above the sunspot umbra. These circumstances indicate the following features of this flare:

i) The flare process involved the strongest magnetic fields above the sunspot umbra that is typical of flares associated with large near-Earth proton enhancements (e.g. Grechnev et al. 2013b).
ii) The magnetic configuration was asymmetrical. To balance the large negative magnetic flux in the strongest-field region above the sunspot, a considerably larger area in weaker positive magnetic fields was required.
iii) The flare brightening above the central part of the S-polarity sunspot umbra indicates the involvement of almost radial magnetic-field lines in the flare process. These long field lines reached considerable heights, and their magnetically conjugate bases were far from the sunspot and the main ribbons. This circumstance explains the presence of remote flare brightenings where the N-polarity predominated.

To calculate the reconnected magnetic flux, we used the radial magnetogram and the contours of flare ribbons identified from UV images. Many AIA 1600 Å images suffered from distortions caused by the bright flare emission. These were saturation and blooming, i.e., charge spreading from saturated pixels to adjacent pixels of the photodetector resulting in spurious expansion of bright features. To reduce these problems, we mostly used AIA 1700 Å images, where the brightness of the ribbons was lower, and the distortions were less pronounced. We manually marked areas of obvious blooming and did not include them in the calculations.

3. Flare Development Based on Nonimaging Observations

3.1. Overall Course of Flare Radio Emission

The total-flux radio emission of the flare was entirely observed by the Nobeyama Radio Polarimeters (NoRP: Torii et al. 1979; Nakajima et al. 1985) at their frequencies of 1, 2, 3.75, 9.4, 17, 35, and 80 GHz. NoRP data seem to be the most reliable and accurate as long as these instruments work properly. Anomalies in their operation are usually easy to detect by visual comparison of temporal profiles recorded at adjacent frequencies. The 80 GHz data for this burst available at the NoRP web site appear incorrect as they show a decrease in the total flux rather than an increase. Besides, the burst at 2 GHz clearly came from a source other than the gyrosynchrotron source, since it was sharply impulsive and much stronger than the bursts at nearby frequencies of 1 and 3.75 GHz at some points during the flare. For these reasons, the frequency sampling of the radio spectrum with NoRP data alone does not appear to be sufficient to analyze it.

Therefore, we additionally used data from the Learmonth station of the US Air Force Radio Solar Telescope Network (RSTN: Guidice 1979; Guidice et al. 1981) that observes the total radio emission at eight fixed frequencies of 245, 410, 610, 1415, 2695, 4995, 8800, and 15400 MHz. The temporal profile recorded at Learmonth at 1.415 GHz differs from those recorded at nearby frequencies and is quite similar to that recorded by NoRP at 2 GHz. This fact confirms the reality of nongyrosynchrotron narrowband emission at frequencies of 1.4 – 2 GHz. Since there is no perfect match between the total fluxes measured at Nobeyama and Learmonth, we recalibrated the Learmonth data in the 2.7 to 15.4 GHz range important for the gyrosynchrotron spectrum based on the NoRP data.

The preburst background levels were subtracted from the NoRP and Learmonth data at 1 GHz and 2.7 GHz to 35 GHz. At each of these frequencies, fluences (temporal integrals of background-subtracted fluxes) were measured within the impulsive phase from 01:25 UT to 01:50 UT. The fluence spectrum measured from NoRP data at frequencies of 1, 3.75, 9.4, 17, and 35 GHz was fitted with a fourth-order polynomial in the log–log space. The correction factors for the Learmonth data from 0.82 to 1.17 were found as the ratios of the values of the fitting function at the corresponding frequencies to the fluences. The Learmonth data at frequencies below 2.7 GHz have not been recalibrated. By interpolating the NoRP data combined with recalibrated Learmonth data the overall radio spectrum of the flare was obtained. It is shown in Figure 3.

As we can see in Figure 3, the impulsive phase started in microwaves at about 01:29 UT and lasted until about 01:45 UT. Broadband gyrosynchrotron emission appears to be dominant at frequencies $\geq$ 3 GHz. Three major peaks are visible around 01:31:00 UT, 01:36:00 UT, and 01:42:00 UT, as well as a minor peak just before 01:30:00 UT. The spectral-maximum frequency of each peak was below 10 GHz, and for the third peak, it was the

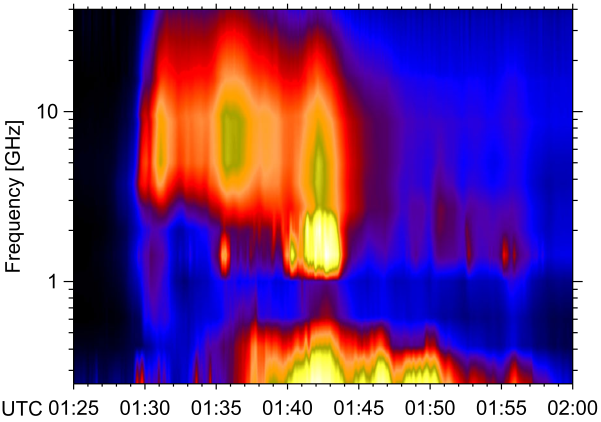

Figure 3 Combined spectrum of the radio burst computed by interpolating fixed-frequency NoRP and recalibrated Learmonth data. Gyrosynchrotron emission is present at frequencies of 3 GHz and higher. Narrowband emission around 1.4 – 2 GHz has a different origin.

lowest. The narrowband emission around 1.4 – 2 GHz had a different origin, probably due to a coherent emission mechanism. The burst visible at frequencies < 700 MHz from 01:37 UT to 01:57 UT was also observed at even lower frequencies (not shown). This low-frequency burst is beyond our scope.

3.2. Temporal Profiles

The HXR burst was observed by RHESSI and by the Konus Gamma-Ray Burst Experiment (Konus: Aptekar et al. 1995) on board the Wind mission (Wind/Konus, sometimes also called Konus–Wind). RHESSI missed the onset and most of the flare because of the night and the passage in the South-Atlantic Anomaly (SAA), where observations had to be interrupted. Wind/Konus observed almost entirely the HXR burst in the waiting mode with reduced spectrum-analysis capabilities.

Figure 4 shows the temporal profiles of the HXR and microwave bursts compared to the magnetic-flux change rate presented in Figure 4a and also smoothed by width five in Figure 4c. The figure also highlights certain features of the bursts and presents some parameters of the microwave emission.

Wind/Konus observed the HXR burst with a sampling interval of 2.944 s from 01:24 UT till 01:44 UT with a gap between 01:32:30 UT and 01:34:00 UT in three broadband energy channels, G1 (18 – 77 keV), G2 (77 – 319 keV), and G3 (319 – 1262 keV). Figure 4b shows the temporal profiles recorded in channels G1 and G2. There is a gradual shoulder (dashed line) under the impulsive component in all three Konus channels. The corresponding background gradual component is visible in the smoothed reconnection rate in Figure 4c, but it is weakly pronounced in the measured reconnection rate in Figure 4a.

RHESSI only observed the last part of the impulsive phase, starting at about 01:39 UT. Resumption of RHESSI observations is indicated by a vertical dashed line in Figure 4b. As Article I demonstrated, the temporal profiles of the last flare peak recorded by RHESSI and Konus in close energy bands were very similar.

In the impulsive phase (after 01:27 UT), there is an approximate correspondence between the peaks in the reconnection rate and the HXR emission. This correspondence also holds for the microwave burst, whose temporal profiles recorded by NoRP are shown in Figure 4d for frequencies of 3.75, 17, and 35 GHz, and in more detail in Figure 4e for 9.4 GHz. On top of the gradual component, three peaks are clearly visible at 01:31 UT, 01:36 UT, and 01:42 UT. The contribution of thermal emission (slowly rising orange curve) to the gradual component

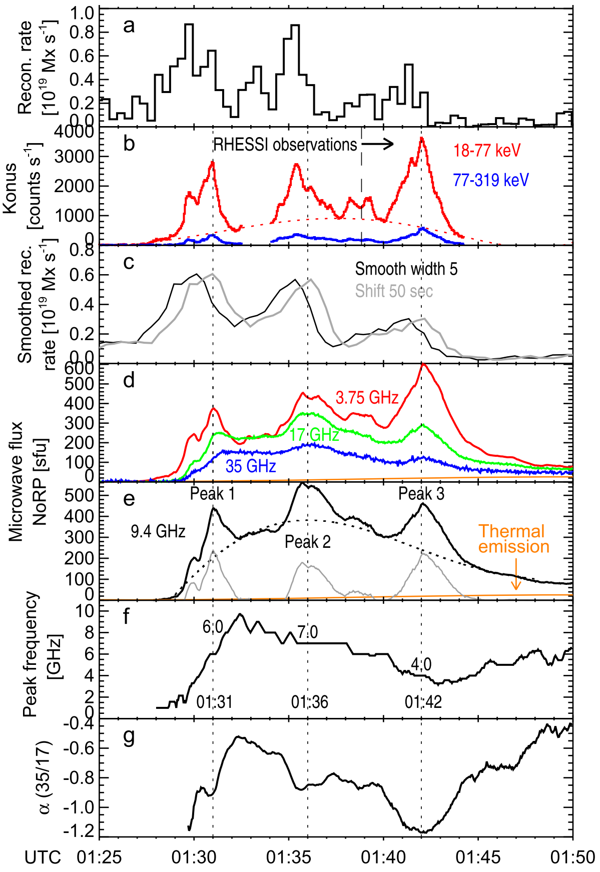

Figure 4 Temporal profiles of the HXR and microwave bursts in comparison with the magnetic-flux change rate (**a**). **b**) Background-subtracted count rates in two HXR Wind/Konus channels recorded with a step of 2.9 s. The *dotted curve* fits the gradual component. The *vertical dashed line* and *arrow* indicate when RHESSI observations resumed. **c**) Magnetic-flux change rate (same as in panel a) smoothed over five neighbors (*black*) and additionally delayed by 50 s (*gray*). **d**) Microwave burst recorded with NoRP at three frequencies of 3.75, 17, and 35 GHz. **e**) NoRP 9.4 GHz data. All NoRP data are averaged over 2.9 s. The *dotted curve* fits the gradual component, and the *gray curves* present the background-subtracted peaks. The *orange curve* in panels d and e presents the optically thin thermal emission computed from GOES soft X-ray data. **f**) Microwave peak frequency computed from NoRP data. **g**) High-frequency microwave spectral index α computed from NoRP data at 17 and 35 GHz.

was negligible during most of the impulsive phase. Comparison of the microwave burst with the HXR burst shows a smoothness of the microwave emission that is noticeable for the double HXR peak between 01:37 UT and 01:39 UT and for peak 3 around 01:42 UT. These features are suggestive of trapping of microwave-emitting electrons.

Comparing the microwave burst with the smoothed reconnection rate in Figure 4c shows that the microwave emission lagged behind the measured reconnection rate by about 50 s. A similar delay may be present in hard X-rays. Delays on the order of tens of seconds between the magnetic-flux change rate and the HXR burst have been found in a number of eruptive events (e.g. Miklenic, Veronig, and Vršnak 2009; Grechnev, Kochanov, and Uralov 2023).

Figure 4f shows the evolution of the microwave peak frequency computed from the NoRP total-flux data by using the second-order fit of the instantaneous log–log spectra (see, e.g., White et al. 2003; Grechnev et al. 2008). For calculations, only frequencies above 2 GHz were used, since the strong, narrowband emission around this frequency was clearly not gyrosynchrotron, as Figure 3 shows. The estimated peak frequency was 6 GHz during the first peak, 7 GHz during the second peak, and 4 GHz during the third peak. The atypically low peak frequency and rather narrow range of its variations are reminiscent of the 26 December 2001 event responsible for GLE63. Analyzing that event, Grechnev et al. (2017a) concluded that the possible reasons for these features were: i) a distributed multiloop microwave-emitting system and ii) asymmetry of the magnetic configuration. The second feature was indeed present in our event (see Section 2).

With such a low peak frequency, 17 GHz seems high enough for the emission to be optically thin. Therefore, it seems possible to estimate the high-frequency slope [α] of the microwave spectrum from the ratio of the total fluxes [S_1] and [S_2] at the highest NoRP frequencies available, $\nu_1 = 17$ GHz and $\nu_2 = 35$ GHz as $\alpha = \log(S_2/S_1)/\log(\nu_2/\nu_1)$. Figure 4g presents the variations of α calculated in this way. Since the microwave spectral slope α is related to the electron energy power-law index [δ'] as $\alpha = 1.22 - 0.9\delta'$ (Dulk and Marsh 1982), the spectrum of microwave-emitting electrons softened during the peaks and hardened afterwards. The power-law index δ' of the electron density spectrum responsible for microwaves is related to the power-law index δ of the electron flux spectrum used in HXR studies as $\delta' = \delta + 0.5$; see, e.g., White et al. 2011. This behavior of the spectral slope is usually explained by the presence of a trap into which continuous injection of electrons occurs (Melrose and Brown 1976; Metcalf and Alexander 1999): The spectrum of the trapped electrons hardens by up to 3/2, whereas the spectrum of newly injected electrons is softer. After 01:45 UT, toward the end of the impulsive phase, the microwave spectrum hardened due to the increasing contribution from thermal emission, which had a flat spectrum. Melnikov and Magun (1998) also proposed the late-stage hardening of the microwave spectrum due to the increasing contribution from the trapped electron population.

However, considering $\delta' = \gamma + 3/2$ with [γ] being the HXR photon index (e.g. White et al. 2011), the expected HXR spectrum is unrealistically hard, mostly with $\gamma < 1$. This is not an exceptional case; a number of studies systematically report that the electron power-law index estimated from microwaves is harder than that estimated from hard X-rays (e.g. Kundu et al. 1994; Silva, Wang, and Gary 2000; White et al. 2011). Several reasons for this discrepancy have been identified. The first reason is the already mentioned hardening of the spectrum of trapped electrons. Second, if the frequency of the observed emission is higher than the peak frequency of the total-flux spectrum, then this does not guarantee that its sources are optically thin (Kundu et al. 2009). Further, as shown by Hannah and Kontar (2011), the relationship between γ and δ' for the thick-target HXR emission changes considerably if an electron beam is not stationary but injected impulsively. Wave-particle interactions further exacerbate the discrepancy.

In summary, both the microwave and HXR bursts followed the magnetic-flux reconnection rate, lagging behind it by several tens of seconds. The shape of the microwave burst was somewhat smoothed relative to the HXR burst. The electron power-law index estimated from microwave data was too hard to be realistic. The peak frequency was low (< 10 GHz), varying in a fairly narrow range. To further elucidate the properties of this microwave burst, the next section examines the spatial structure of its sources.

4. Spatial Structure of Microwave Sources

The Nobeyama Radioheliograph (NoRH: Nakajima et al. 1994) performed microwave imaging observations of the flare at two frequencies of 17 and 34 GHz. In analyzing the spatial structure of microwave sources, we compared images produced by NoRH with flare structures visible in EUV. For this purpose, we used images obtained by SDO/AIA in the 94 Å channel that is little affected by overexposure distortions. This EUV channel has a characteristic temperature of 6.3 MK and a weaker-sensitivity window around 1 MK (Lemen et al. 2012).

EUV images present column emission measure distributions of the coronal plasma with temperatures falling within the temperature-sensitivity region of the given AIA channel. Microwave images present column density distributions of accelerated electrons in the corona, whose emissivity strongly depends on the magnetic field (Dulk and Marsh 1982). Emissions in these two spectral domains reflect different processes and are determined by different physical quantities, so their coincidence is not expected. Time also plays a role - bombardment of the chromosphere by accelerated electrons causes its heating, and the heated plasma fills coronal magnetic structures, where it cools and only then appears in the given EUV channel, according to the temperature sensitivity of this channel. In addition, EUV telescopes using focusing optics have considerably higher spatial resolution and dynamic range than Fourier-synthesis radio telescopes. Taking into account all these differences, we will try to understand whether acceleration and thermal processes develop in the same or in different coronal structures.

To analyze the spatial structure of microwave sources, we synthesized image sets from NoRH data using standard imaging software. One-second snapshots were produced in steps of ten seconds from 01:20 UT to 01:50 UT, covering the impulsive phase. We used hanaoka software to synthesize 34 GHz images and enhanced-resolution fujiki software to synthesize 17 GHz images. During the flare, the NoRH beam had an almost circular cross-section and a full width at half-maximum of $\approx 13''$ at 17 GHz and $\approx 8.5''$ at 34 GHz. We also used later-stage images available at solar.nro.nao.ac.jp/norh/images/event/20120517_0141 in subdirectories steady_hanaoka/ and steady_fujiki/. All microwave images in both sets were coaligned with each other and with AIA 94 Å images as accurately as possible.

Figure 5 compares images of several event milestones observed by AIA in 94 Å and by NoRH at 34 GHz and 17 GHz. The event stages are indicated in the left-column panels, which show AIA 94 Å images in the logarithmic brightness scale. When comparing them with microwave images, we used the same method as Grechnev et al. (2017a), i.e., to compensate for the difference in spatial resolution, we convolved the AIA images ($0.6''$ resolution) with the NoRH beam at 34 GHz. The square roots from convolved AIA images are shown in the second column. The next two columns show the square roots of the simultaneous NoRH images at 34 and 17 GHz, except in the top-right panel, where the contours of the NoRH 17 GHz image are superimposed on the SDO/HMI intensitygram. The aia94_conv_norh.mpg movie in the electronic supplementary material presents a more detailed comparison of these images from 01:20 UT to 01:50 UT.

The 17 GHz preflare image was dominated by a northern negatively polarized (x-mode) source located above the sunspot. Its brightness temperature at 17 GHz was 0.39 MK at 01:20 UT and increased to 0.54 MK at 01:25 UT. The degree of polarization at both times was -0.2. The properties of this source indicate its gyromagnetic emission mechanism. Therefore this source did not appear in EUV, but in microwaves, it persisted throughout the flare when its emission was clearly gyrosynchrotron. This source was strongest during the third peak, when its brightness temperature reached 18 MK at 17 GHz, 3.9 MK at 34 GHz, and the average degree of polarization at 17 GHz was -0.05. This source was also observed after the end of the impulsive phase, but only at 17 GHz. Its brightness temperature 40 minutes later, in the bottom-right panel, was almost 1 MK.

Apart from the source above the sunspot, the rest of the microwave-emitting system generally matched the position and outline of the complex structure visible in EUV. There is no complete correspondence between the brightness distributions in microwave and EUV images, since emissivity in microwaves depends on magnetic field, whereas in EUV it does not. The 94 Å images reveal only part of the arcade of hot flare loops, whose bases were located on the ribbons traced by elongated bright structures directed from SSW to NNE.

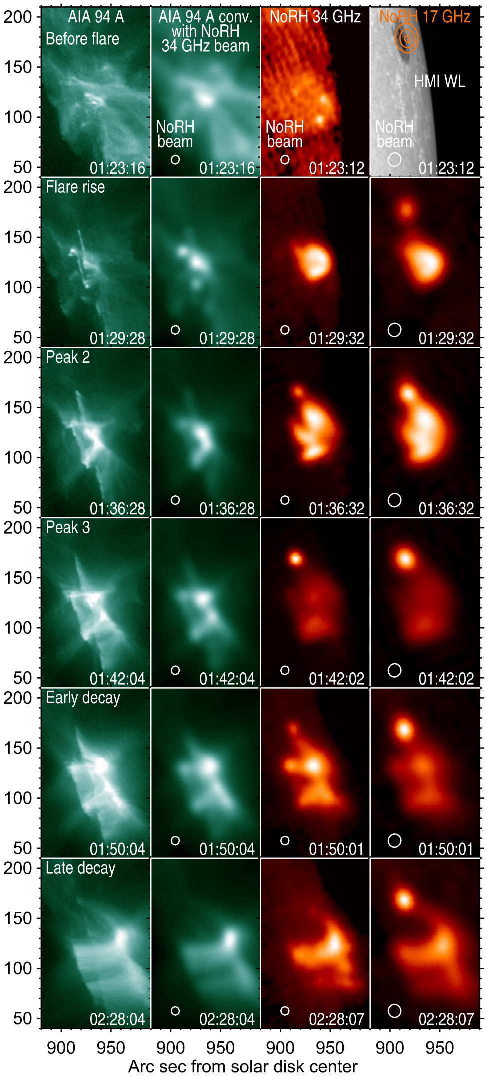

Figure 5 Spatial structure of the microwave-emitting system in comparison with the flare arcade observed by SDO/AIA in 94 Å. *Left column*: original AIA 94 Å images. *Second column from left*: AIA 94 Å images convolved with the NoRH 34 GHz beam. *Third column from left*: NoRH 34 GHz images. *Right column*: NoRH 17 GHz images. The *background* in the upper-right panel presents the contours of the NoRH 17 GHz image overlaid on the SDO/HMI intensitygram. The *small ellipse* in the lower-left corner of each panel (except for the left column) represents the half-height contour of the NoRH beam at the corresponding frequency.

The entire volume of the arcade in the microwave images was filled with accelerated electrons during the flare. The brightness temperature of the arcade was mainly in the range of 2 – 10 MK at 17 GHz and 0.5 – 3 MK at 34 GHz during most of the burst.

Comparison with the EUV images in the bottom two rows of Figure 5 shows that the increased brightness of the arcade top in the microwave images was due to the overlap of the arcade loops along the line of sight. As the flare progressed, the loops gradually filled with evaporated hot plasma. The contribution of thermal bremsstrahlung to the arcade emission gradually increased and became dominant in the images of the bottom row, as evidenced by the closeness of the total fluxes estimated for the arcade from the images at 17 and 34 GHz, corresponding to this time. Similar gradual changes in the appearance of the arcade in both EUV and microwave images indicate that both thermal and nonthermal processes occurred in the same configuration.

Figure 6 Eight preflare and flare impulsive-phase episodes, observed simultaneously by SDO/AIA in 94 Å (*background*) and by NoRH at 17 GHz (*cyan contours*) and at 34 GHz (*orange contours*). Contour levels are [0.05, 0.1, 0.2, 0.4, 0.8] of the maximum brightness temperature of each microwave image.

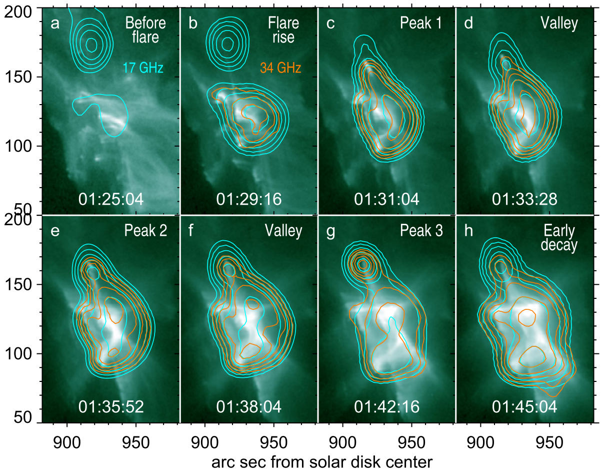

A more detailed comparison of the microwave and EUV images is shown in Figure 6, which presents the flare onset and some episodes of the impulsive phase observed by AIA in 94 Å (background), with cyan contours of NoRH 17 GHz images and orange contours of NoRH 34 GHz images superimposed on them (see also the `aia94_norh_cont.mpg` movie in the electronic supplementary material). In the 34 GHz preflare image, the active region was not reliably identified, so there are no corresponding contours. From the onset of the impulsive phase, the microwave-emitting system at both 17 and 34 GHz generally matched the outline of the configuration observed in 94 Å, given the difference in spatial resolution of NoRH and AIA. During both the peaks and the valleys between them, the entire multiloop flare arcade, as well as the northern source located above the sunspot, emitted microwaves without significant differences between these episodes.

As noted, this flare resembled the SOL2001-12-26 event in terms of the asymmetry of the magnetic configuration and parameters of the microwave burst. For that event, Grechnev et al. (2017a) inferred that, despite the apparent simplicity of the structure visible in microwave images, the actual source of the microwave emission was a distributed multiloop system. This section has demonstrated that microwave images of the 17 May 2012 flare directly presented a complex microwave-emitting structure filled with accelerated electrons. This structure comprised the entire flare arcade and a separate gyrosynchrotron source located above the sunspot, whose magnetic fields were involved in the flare process.

5. Hard X-ray and Microwave Spectra

5.1. Hard X-ray Spectra

As noted in Section 3.2, Wind/Konus operated in the waiting mode and observed the HXR burst almost entirely. In this mode the capabilities of spectral analysis are limited by the presence of only three broadband channels, G1, G2, and G3. The last peak around 01:42 UT was also fully observed by RHESSI, whose spectrometric capabilities were normal. First, we examined the spectrum of this HXR peak using the RHESSI data, and then we used the Konus data.

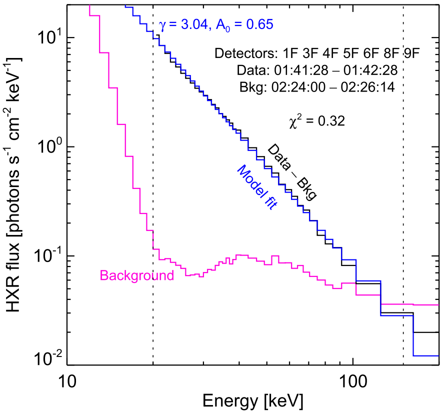

Figure 7 HXR spectrum calculated from the background-subtracted RHESSI data (*black*) and its fit with a single power-law function (*blue*) in the energy interval 20 – 150 keV bounded by the *vertical dotted lines*.

A nonobvious task in calculating the HXR spectrum from RHESSI data is to subtract the background, whose level varied as the spacecraft moved in its orbit. Because the flare began outside RHESSI observations, the preflare background level is unknown. We used the background after the burst in the interval 02:24 – 02:26 UT, when its level reached maximum in this orbit. Judging by our fitting of orbital background variations, their possible underestimation was $< 10\%$ in the energy range of 50 – 100 keV and $< 25\%$ in the range of 100 – 300 keV.

We measured the spectrum from RHESSI data by means of the Object Spectral Executive software (OSPEX: Tolbert and Schwartz 2020), which is an object-oriented interface for spectral analysis of solar X-ray data. To calculate the spectrum for the last HXR peak around 01:42 UT, we chose the accumulation time from 01:41:28 UT to 01:42:28 UT. Since this interval corresponds to the rise phase of thermal emission and the background interval corresponds to its decay phase, the low-energy thermal part of the spectrum calculated from data with the background subtracted in this way does not make sense. Therefore, we fitted the spectrum only in the energy range from 20 to 150 keV. Figure 7 shows the result. Having also considered the background shortly after the burst, we estimated the photon power-law index of the last HXR peak and its uncertainty, measured from RHESSI data, to be $\gamma = 3.00 \pm 0.07$.

To measure the HXR spectrum from Wind/Konus data, we used An X-Ray Spectral Fitting Package (XSPEC: Arnaud 1996). In this case, due to the location of the instrument at the Lagrangian point L1, the background level was stable. It was possible to calculate the HXR spectrum for most of the impulsive phase. The power-law indices we estimated are 3.55 ± 0.05 for the first peak and 3.40 ± 0.05 for both the second and third peaks. The power-law index estimated for the gradual component (the red-dotted line in Figure 4b) is 3.54 ± 0.20.

Comparison with the results obtained from the RHESSI data in steps of four seconds in the interval 01:39 – 01:44 UT, when both instruments were observing, showed similar variations in the estimated power-law indices, but the estimates from the Konus data were systematically softer by about 0.4 than those obtained from the RHESSI data. This discrepancy seems unexpected, since the previous estimates obtained with these two instruments operating in the same observing modes were consistent with each other (e.g. Glesener and Fleishman 2018). Analysis of the situation led us to the conclusion that this mismatch was due to the difference in the characteristics of the two instruments. This is a large excess of the energy range covered by the broadband Konus channels (18 – 77 keV, 77 – 319 keV, and

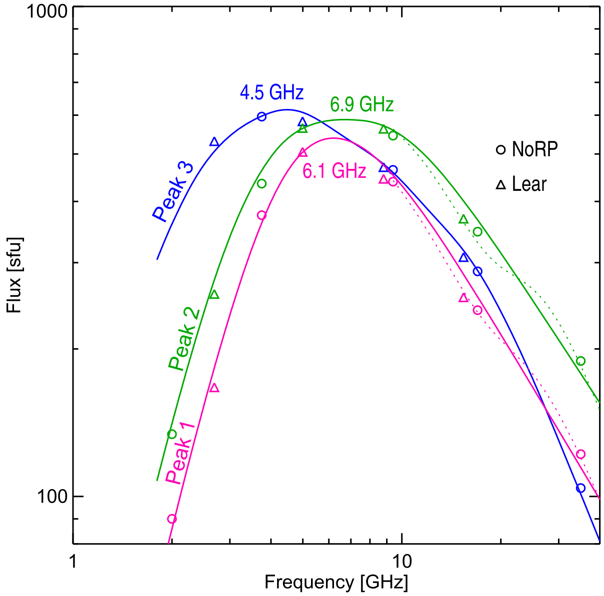

Figure 8 Gyrosynchrotron spectra observed during the three peaks of the microwave burst (*symbols*) and their modeling (*color curves*). Different *colors* correspond to different peaks. The *symbols* represent the measurements from NoRP data (*circles*) and from recalibrated Learmonth data (*triangles*). The *dotted lines* represent the high-frequency parts of the hypothetical spectra of peaks 1 and 2 with a steeper slope discussed in the text. The spectral-maximum frequency obtained in the modeling is indicated for each of the three peaks.

319 – 1262 keV) over the range analyzed using the RHESSI data. A thermal contribution in the Konus G1 channel cannot be ruled out, but according to our assessment, it is unlikely to have been significant. Thus the real HXR spectrum at high energies was probably steeper than in the 20 – 150 keV region. The spectrum might have had above 200 keV a rollover or break if its shape was a double power-law.

5.2. Microwave Spectra

To analyze microwave spectra, we used NoRP and recalibrated Learmonth data (see Section 3.1 and Figure 3). Symbols of different colors in Figure 8 present the fluxes measured from fixed-frequency observations during the three microwave peaks. Here we subtracted the contribution of thermal bremsstrahlung that was noticeable during the third peak, especially at 35 GHz. The accuracy of these measurements is unknown, and we do not consider them to be perfect.

Let us first look at the third peak, for which the data are the most certain. From the flux ratio at 17 and 35 GHz with the thermal contribution subtracted, we estimated the microwave spectral index $\alpha \approx -1.4$, which corresponds to the electron energy power-law index $\delta' \approx 2.9$ (Dulk and Marsh 1982). On the other hand, its estimate from the RHESSI data gives $\delta' = \gamma + 1.5 = 4.50 \pm 0.07$ and even steeper from the Wind/Konus data. Hardening of the spectrum of microwave-emitting electrons ($>$ 100 keV) held in a trap is possible if they are injected into the trap continuously for a sufficiently long time. In this case, we would expect that the electrons gradually precipitating out of the trap would produce a harder component of the HXR spectrum, detectable at higher energies. However, the estimates from the Wind/Konus data indicate that, on the contrary, at higher energies the spectrum becomes softer.

The power-law index of the gradual component of the HXR burst differed little from that of the impulsive component. Therefore, the presence of the gradual component either does not support the hardening of the spectrum of electrons continuously injected into the trap.

Since the third peak was the last one in the burst, the influence of trapping effects in case of possible continuous injection would be the greatest for the third peak among all the peaks. However, this influence was not detected even in the third peak. Thus the hardening of the spectrum of trapped electrons, invoked to explain the long-known discrepancy between the estimates of the electron spectrum obtained from HXR and microwave data, is not confirmed here. Although there are signs of trapping of microwave-emitting electrons (Section 3.2 and Figures 4b – 4d), the trapping time was probably insufficient to harden their spectrum. There may be other reasons for this discrepancy, such as inaccuracies in the thick-target model for impulsive injection and the wave-particle interaction proposed by Hannah and Kontar (2011). Also, it cannot yet be ruled out that the spectrum above 35 GHz was steeper.

For better understanding, it would be beneficial to reconstruct at least the total-flux spectrum at frequencies where there are no images. As shown in Section 4, the microwave-emitting system comprised the entire multiloop flare arcade and a compact source above the sunspot. Given the circular cross-section of each loop, the smallest number of loops existing simultaneously was at least about the length-to-width ratio of the ribbon, here roughly 20. The problem is to calculate the total microwave emission of multiple coronal loops, each of which is an extended source with a nonuniform distribution of parameters along its length. The most advanced research tool, the GX Simulator (Nita et al. 2023), allows us to model the gyrosynchrotron emission of an inhomogeneous source with various electron distributions based on a real magnetogram, as well as other capabilities. The GX Simulator allows us to model the spectrum of the gyrosynchrotron emission from a few flare loops, but each loop should be defined manually, which does not look feasible for two dozen loops. The modeling is further complicated by the discrepancy between the HXR and microwave spectra.

Faced with the difficulties of modeling the microwave emission of the flare arcade, Grechnev et al. (2017a) applied a simplified approach based on an approximate analytical description of the gyrosynchrotron emission developed by Dulk and Marsh (1982). Each microwave-emitting loop is replaced by a pair of homogeneous cubic sources located in its legs, which are rooted in both opposite-polarity ribbons. Each source has an individual volume and magnetic-field strength estimated using the radial magnetic-field distribution on the photosphere and the balance of magnetic fluxes at the conjugate bases of the loop. The procedure for splitting the ribbons into model sources progresses from one end of the ribbons to the other, thus connecting the magnetically conjugate sources. This allows pairs of sources to be formed without overlapping loops. The number of resulting loops is close to the length-to-width ratio of the ribbon (here 18). Then the magnetic-field strengths are scaled to the coronal values using a constant factor estimated by referring to Lee, Nita, and Gary (2009). The total flux is calculated as the sum of the fluxes emitted by all paired sources.

The model was first described in detail by Grechnev et al. (2017a). There were no HXR data in that case. The refined model was used by Grechnev et al. (2020) in the study of another event, where a comparison was made with HXR spectra; trapping was unlikely to be significant. The electron energy power-law indices δ' needed to model the microwave spectra of the flare peaks were found to be 0.76 – 0.93 harder than those estimated from the HXR spectra.

In our event the discrepancy between the estimates from microwave and HXR data is even greater, so we tried to reproduce the microwave spectra without reference to hard X-rays. We used the radial magnetic-field distribution, a part of which with the strongest fields up to $[-2540, 1130]$ G is shown in Figure 2c. The source above the sunspot was modeled as a separate gyrosynchrotron source. During the third peak, this source was well separated from the arcade in the NoRH images, allowing its parameters to be measured. Its contribution to the total flux was about 30% at 17 GHz and 20% at 34 GHz, and from its flux ratio calculated from the images we estimated $\delta' \approx 3.23$, which we also used for the arcade. With these additional constraints, we obtained the spectrum for the third peak, shown in blue in Figure 8. Here the difference between the δ' value used in the modeling and the estimate from the HXR data does not exceed two, as previously reported (e.g. Silva, Wang, and Gary 2000; White et al. 2011).

During peaks 1 and 2, the source above the sunspot is more difficult to separate from the arcade in the NoRH images. We can only state that its contribution to the total flux here was less than in the third peak. This source is not suitable for estimating δ' in this case. To model the spectra during these peaks, we had to rely on the ratio of the total fluxes at 17 and 35 GHz. These spectra are shown in Figure 8 in pink for peak 1 and in green for peak 2. The dotted lines present hypothetical spectra whose slopes at high frequencies might be closer to those estimated from HXR data. These hypothetical spectra were modeled by assigning the sunspot-source contributions of about 20% at 17 GHz and 55% at 34 GHz, which contradict the estimates from the NoRH images. So these spectra are unrealistic.

The differences of all modeled spectra from the measured fluxes do not exceed ±7% for the NoRP data and ±12% for the recalibrated Learmonth data and seem to be consistent with the probable measurement errors and existing uncertainties. Leaving aside the large discrepancy between the high-frequency slopes and the estimates from the HXR spectra in the first two peaks, we focused on the overall shape of the microwave spectra. As noted by Grechnev et al. (2017a), in an asymmetric magnetic configuration, the magnetic-flux balance requires larger areas on the weaker field side, resulting in a higher low-frequency part of the spectrum. This broadens the spectrum and shifts its peak frequency to the left. These features are inherent in all three spectra in Figure 8. The peak frequencies of the model spectra are close to the values indicated in Figure 4f.

6. Discussion

The presented analysis revealed similarities between a number of properties of this flare and the SOL2001-12-26 flare (Grechnev et al. 2017a). This applies, for example, to the GOES importance of the flares, M5.1 here vs. M7.1 in the 26 December 2001 event. Both flare sites were close to a well-connected position, N06 W78 here vs. N08 W54. There was also a similarity in their morphology.

As is typical for a flare associated with a major SEP event, the flare process on 17 May 2012 involved the strongest magnetic fields above the sunspot umbra (Grechnev et al. 2013b). The same was observed in the 26 December 2001 flare. This morphological feature hints at the possibility of a high reconnection rate. The maximum magnetic-flux change rate measured in our event with an interval of 24 s and smoothed by width three was $6.8 \times 10^{18}\,\mathrm{Mx\,s^{-1}}$ (cf. Figures 4a and 4c; see Article I). This value is close to the statistical estimate for the M5.1 GOES importance of our flare, $5.3 \times 10^{18}\,\mathrm{Mx\,s^{-1}}$, obtained by Tschernitz et al. (2018) from one-minute observations (their Table 4 and Figure 7b). Flares of comparable size are present in the Fermi/LAT catalog of flares, in which acceleration of protons to high energies has been established (Tables 1 and 3 in Ajello et al. 2021).

However, the majority of the flares in this catalog are of GOES X class. According to Tschernitz et al. (2018), the lower GOES importance of the 17 May 2012 and 26 December 2001 flares implies a lower reconnection rate in these two flares compared to most flares listed in the LAT catalog. This is also consistent with the facts that: i) these two flares were the least powerful among the GLE-related flares of recent decades and ii) the microwave bursts in these two events were considerably weaker than in a typical SEP-related flare.

Unlike typical SEP-related microwave bursts with peak frequencies exceeding 10 GHz, the bursts in the two events had broad microwave spectra and the narrow range of the peak-frequency variations from 5 to 7 GHz in the 26 December 2001 flare and similar values in our event (Figures 4f and 8). The differences in the properties of our event from the typical situation are even greater than those in the 26 December 2001 event. The question arises as to what explains these peculiarities of our event. To find an explanation, we compare these two flares with a pair of GLE-associated flares, SOL2005-01-20 (GLE69, Grechnev et al. 2008) and SOL2006-12-13 (GLE70, Grechnev et al. 2013a), which were accompanied by typical strong microwave bursts ($> 10^4$ sfu) with high peak frequencies exceeding 10 GHz.

In typical GLE-related X-class flares, both flare ribbons were located above the opposite-polarity sunspot umbrae. Thus the microwave sources at the legs of the flare arcade were in the strongest magnetic fields and had considerable areas. Because of this, the microwave fluxes and peak frequencies reached high values. In the SOL2001-12-26 flare, one ribbon was located above the sunspot umbra, and the other above the penumbra, where the magnetic fields were not the strongest but still high. Because of this, the microwave flux was considerably lower, and the asymmetry of the magnetic configuration led to a broadening of the microwave spectrum and a lower peak frequency, as discussed above. In our event, only a compact source was observed at 17 and 34 GHz above the sunspot umbra, whereas the flare arcade was rooted in moderate magnetic fields. The contribution of the compact source above the sunspot to the total flux was less than the contribution of the extended arcade.

Around the peak of the burst on 26 December 2001, two microwave sources of comparable brightness and area were observed in the arcade legs. At 17 GHz the flux reached 1780 sfu, and the brightness temperature [T_B] reached 62 MK. In the 17 May 2012 flare, at 17 GHz the flux reached 360 sfu, T_B reached 18 MK in the source above the sunspot, and the arcade had $T_\mathrm{B} \approx 2 - 10$ MK. This moderate range of brightness temperatures made it possible to discern the structure of the microwave-emitting region, in which the arcade and the source above the sunspot were identified. This opportunity is related to instrumental limitations.

According to Masuda, Kosugi, and Hudson (2001) and Krucker et al. (2014), the reasons for the simplicity and compactness of nonthermal sources observed in HXR and γ-rays, noted in Section 1, are the limited sensitivity and dynamic range (typically 5 – 10, sometimes up to ≈ 30) of the Fourier-synthesis HXR imagers. This is caused by poor coverage of the (u, v)-plane. Therefore the sources weaker than 10% of the brightest one are usually not detected in their images.

Microwave images of flares have been acquired almost exclusively by interferometers, also using Fourier synthesis (mainly NoRH). Their coverage of the (u, v)-plane is considerably better than that of HXR imagers. However, as Grechnev et al. (2017a) demonstrated, the strong dependence of optically thin gyrosynchrotron emission on the magnetic field makes their capabilities for detecting weak nonthermal sources comparable to those of HXR imagers, whereas the spatial resolution in microwaves is inherently poorer. Thus observations leave the impression that nonthermal manifestations are confined to compact configurations, although in reality, they may be closely related to those observed in thermal emissions. Zimovets, Kuznetsov, and Struminsky (2013) came to a similar conclusion. The 17 May 2012 flare has provided a rare opportunity to establish a complete correspondence between the configurations in which thermal and nonthermal processes developed. A link has been found between the microwave manifestations of the flare and magnetic reconnection that was associated with eruptions, as demonstrated in Article I.

Given that the flare and the eruptions that eventually led to the CME were interconnected by the same reconnection processes, we can speculate about their consequences on particle acceleration. The intensity of flare processes is determined by the rate of change of the magnetic flux, whereas the CME speed is determined by the total reconnected flux (Vršnak 2016; Pal et al. 2018). If the CME is fast, then a bow shock will eventually form in front of it. Acceleration of SEP protons is possible both by flare processes and by shock waves. These mechanisms and locations of particle acceleration are different, although their underlying causes are interrelated. Therefore it seems possible that there is an indirect correlation between the parameters of particles accelerated by these two different mechanisms, which corresponds to the idea of the "big flare syndrome" (Kahler 1982) mentioned in Section 1. We can try to find indications of the source of the SEP protons from the parameters of their spectra.

The shape of the spectrum of a near-Earth proton enhancement is close to a broken double power-law with a break energy in the range of about 2 – 46 MeV and a steeper slope above the break (e.g. Mewaldt et al. 2012). At the highest energies observed in GLEs (> 400 MeV), the slope is even steeper (e.g. Miroshnichenko, Vashenyuk, and Pérez-Peraza 2013). Having analyzed the time-of-maximum integral flux spectra for a number of proton events, Kiselev, Meshalkina, and Grechnev (2022) found a high correlation between their slopes above the break energy (roughly between 50 and 400 MeV) [γ_{p2i}] and the power-law indices of the photon spectra [γ_{HXR}] (mostly between 50 and 200 keV) in the associated flares, described by the regression equation $\gamma_{\mathrm{p2i}} = (1.85 \pm 0.19)\gamma_{\mathrm{HXR}} - (3.81 \pm 0.67)$. No correlation was found between γ_{p2i} and CME speeds.

Let us apply this regression equation, neglecting all errors, to the 17 May 2012 event. We take the γ_{HXR} estimates in Section 5.1 of 3.0 from the RHESSI data and 3.5 from the Wind/Konus data as bounds for the comparable energy range 50 – 200 keV. Considering that the differential spectrum is steeper than the power-law integral spectrum by one, we estimate the expected index of the corresponding differential proton spectrum $\gamma_{\mathrm{p2}} \approx \gamma_{\mathrm{p2i}} + 1$ from 2.74 to 3.67. The slope of the event-integrated fluence spectrum actually measured for this proton event in the Payload for Antimatter–Matter Exploration and Light-nuclei Astrophysics (PAMELA) experiment was 2.42 ± 0.14 for the Ellison–Ramaty fit (power-law with an exponential rollover) and 3.03 ± 0.04 for the power-law fit (Bruno et al. 2018, Figure 3). The presumable ranges of expected and actual values of the proton power-law index overlap even without considering any errors.

Kiselev, Meshalkina, and Grechnev (2022) also found a high anticorrelation between the slopes of the integral proton spectra below the break energy [γ_{p1i}] and the plane-of-the-sky CME speeds [V_{CME}] with a regression equation $\gamma_{\mathrm{p1i}} = (-12.39 \pm 1.89) \times 10^{-5} V_{\mathrm{CME}} + (0.89 \pm 0.04)$. No correlation was found between γ_{p1i} and γ_{HXR}. With the speed of the relevant CME of 1580 $\mathrm{km\,s^{-1}}$ according to the online CME catalog (cdaw.gsfc.nasa.gov/CME_list/: Yashiro et al. 2004), from this regression equation we estimate the lowest-energy slope of the differential spectrum $\gamma_{\mathrm{p1}} \approx 1.7$, which is clearly flatter than that above the break energy, γ_{p2}. This shape is consistent with the spectrum of this event given by Cohen and Mewaldt (2018) in their Figures 4 and 6, where the break occurs at about 1 – 2 MeV. The estimate of 1.7 is close to the values listed by Mewaldt et al. (2012) for GLE events of Solar Cycle 23. Thus the 17 May 2012 event appears to fit into these statistical patterns.

These patterns suggest a statistical predominance of the acceleration of the most numerous lower-energy protons by CME-driven bow shocks and the acceleration of higher-energy protons by flare processes. The spectra of the highest-energy GLE protons, for which Kiselev, Meshalkina, and Grechnev (2022) did not find any correlation with either hard X-rays or the CME speeds, are probably strongly influenced by transport effects (Dalla et al. 2020). Despite all the existing uncertainties, the above considerations and estimates indicate that none of the possible sources of accelerated SEP protons should be ignored.

Supplementary Information The online version contains supplementary material available at https://doi.org/10.1007/s11207-025-02437-9.

Acknowledgements We thank A.A. Kochanov and D.D. Frederiks for fruitful discussions. We thank the anonymous reviewer for useful remarks. We appreciate the NASA/SDO and the AIA and HMI science teams, the teams that operated RHESSI, the Nobeyama solar facilities, and the USAF RSTN Network. We thank the Wind/Konus team at the Ioffe Institute. We also thank the team maintaining the CME Catalog at the CDAW Data Center by NASA and The Catholic University of America in cooperation with the Naval Research Laboratory. SOHO is a project of international cooperation between ESA and NASA.

Author contributions N.M. synthesized and formerly analyzed the NoRH images, processed and analyzed RHESSI data. A.L. restored and analyzed Wind/Konus data. A.U. developed the model of gyrosynchrotron emission of a multiloop system and participated in the interpretation of observations. V.K. updated the model, measured the reconnected magnetic flux, and modeled microwave spectra. V.G. coordinated the study, performed other measurements, and drafted the manuscript. All authors discussed the results and reviewed the manuscript.

Funding This study was financially supported by the Ministry of Science and Higher Education of the Russian Federation. A.L. Lysenko was supported by the basic funding program of the Ioffe Institute No. FFUG-2024-0002.

Data Availability The datasets analyzed during the current study were derived from the following public domain resources: Joint Science Operations Center jsoc.stanford.edu/ Virtual Solar Observatory sdac.virtualsolar.org/ Nobeyama Radioheliograph solar.nro.nao.ac.jp/norh/ Nobeyama Radio Polarimeters solar.nro.nao.ac.jp/norp/ RSTN data ftp://ftp.ngdc.noaa.gov/STP/space-weather/solar-data/solar-features/solar-radio/ National Centers for Environmental Information www.ncei.noaa.gov/data/goes-space-environment-monitor/ SOHO LASCO CME CATALOG cdaw.gsfc.nasa.gov/CME_list/ The Wind/Konus waiting-mode data used in this study are available from A.L. Lysenko on reasonable request. The NoRH data sets synthesized for this study are available from the corresponding author on reasonable request.

Declarations

Competing interests The authors declare no competing interests.

References

Ajello, M., Baldini, L., Bastieri, D., Bellazzini, R., Berretta, A., Bissaldi, E., Blandford, R.D., Bonino, R., Bruel, P., Buson, S., et al.: 2021, First Fermi-LAT solar flare catalog. *Astrophys. J. Suppl.* **252**, 13. DOI. ADS.

Akinian, S.T., Alibegov, M.M., Kozlovskii, V.D., Chertok, I.M.: 1978, On quantitative diagnostics of proton bursts from characteristics of microwave radio bursts at ≈9 GHz frequency. *Geomagn. Aeron.* **18**, 410. ADS.

Anastasiadis, A., Lario, D., Papaioannou, A., Kouloumvakos, A., Vourlidas, A.: 2019, Solar energetic particles in the inner heliosphere: status and open questions. *Phil. Trans. Roy. Soc. London Ser. A, Math. Phys. Sci.* **377**, 20180100. DOI. ADS.

Aptekar, R.L., Frederiks, D.D., Golenetskii, S.V., Ilynskii, V.N., Mazets, E.P., Panov, V.N., Sokolova, Z.J., Terekhov, M.M., Sheshin, L.O., Cline, T.L., Stilwell, D.E.: 1995, Konus-W gamma-ray burst experiment for the GGS Wind spacecraft. *Space Sci. Rev.* **71**, 265. DOI. ADS

Arnaud, K.A.: 1996, XSPEC: the first ten years. In: Jacoby, G.H., Barnes, J. (eds.) *Astron. Data Anal. Software and Sys. V, Astron. Soc. Pacific Conf. Ser.* **101**, 17. ADS.

Atwood, W.B., Abdo, A.A., Ackermann, M., Althouse, W., Anderson, B., Axelsson, M., Baldini, L., Ballet, J., Band, D.L., Barbiellini, G., et al.: 2009, The Large Area Telescope on the Fermi gamma-ray space telescope mission. *Astrophys. J.* **697**, 1071. DOI. ADS.

Aulanier, G., Janvier, M., Schmieder, B.: 2012, The standard flare model in three dimensions. I. Strong-to-weak shear transition in post-flare loops. *Astron. Astrophys.* **543**, A110. DOI. ADS.

Bain, H.M., Krucker, S., Glesener, L., Lin, R.P.: 2012, Radio imaging of shock-accelerated electrons associated with an erupting plasmoid on 2010 November 3. *Astrophys. J.* **750**, 44. DOI. ADS.

Bruno, A., Bazilevskaya, G.A., Boezio, M., Christian, E.R., de Nolfo, G.A., Martucci, M., Merge', M., Mikhailov, V.V., Munini, R., Richardson, I.G., et al.: 2018, Solar energetic particle events observed by the PAMELA mission. *Astrophys. J.* **862**, 97. DOI. ADS.

Carmichael, H.: 1964, *A process for flares* **50**, NASA, Science and Technical Information Division, Washington DC, 451. ADS.

Castelli, J.P., Barron, W.R.: 1977, A catalog of solar radio bursts 1966–1976 having spectral characteristics predictive of proton activity. *J. Geophys. Res.* **82**, 1275. DOI. ADS.

Cliver, E.W.: 2006, The unusual relativistic solar proton events of 1979 August 21 and 1981 May 10. *Astrophys. J.* **639**, 1206. DOI. ADS.

Cohen, C.M.S., Mewaldt, R.A.: 2018, The ground-level enhancement event of September 2017 and other large solar energetic particle events of cycle 24. *Space Weather* **16**, 1616. DOI. ADS.

Costa, J.E.R., Simões, P.J.d.A., Pinto, T.S.N., Melnikov, V.F.: 2013, Solar burst analysis with 3D loop models. *Publ. Astron. Soc. Japan* **65**, S5. DOI. ADS.

Croom, D.L.: 1971, Forecasting the intensity of solar proton events from the time characteristics of solar microwave bursts. *Solar Phys.* **19**, 171. DOI. ADS.

Dalla, S., de Nolfo, G.A., Bruno, A., Giacalone, J., Laitinen, T., Thomas, S., Battarbee, M., Marsh, M.S.: 2020, 3D propagation of relativistic solar protons through interplanetary space. *Astron. Astrophys.* **639**, A105. DOI. ADS.

Dierckxsens, M., Tziotziou, K., Dalla, S., Patsou, I., Marsh, M.S., Crosby, N.B., Malandraki, O., Tsiropoula, G.: 2015, Relationship between solar energetic particles and properties of flares and CMEs: statistical analysis of solar cycle 23 events. *Solar Phys.* **290**, 841. DOI. ADS.

Dulk, G.A., Marsh, K.A.: 1982, Simplified expressions for the gyrosynchrotron radiation from mildly relativistic, nonthermal and thermal electrons. *Astrophys. J.* **259**, 350. DOI. ADS.

Firoz, K.A., Gan, W.Q., Li, Y.P., Rodríguez-Pacheco, J., Su, Y.: 2017, On the time evolution of brightness, volume and height of a coronal source in an M-class flare. *Astrophys. Space Sci.* **362**, 113. DOI. ADS.

Forrest, D.J., Chupp, E.L.: 1983, Simultaneous acceleration of electrons and ions in solar flares. *Nature* **305**, 291. DOI. ADS.

Forrest, D.J., Vestrand, W.T., Chupp, E.L., Rieger, E., Cooper, J., Share, G.H.: 1986, Very energetic gamma-rays from the 3 June 1982 solar flare. *Adv. Space Res.* **6**, 115. DOI. ADS.

Glesener, L., Fleishman, G.D.: 2018, Electron acceleration and jet-facilitated escape in an M-class solar flare on 2002 August 19. *Astrophys. J.* **867**, 84. DOI. ADS.

Gopalswamy, N., Xie, H., Akiyama, S., Yashiro, S., Usoskin, I.G., Davila, J.M.: 2013b, The first ground level enhancement event of solar cycle 24: direct observation of shock formation and particle release heights. *Astrophys. J. Lett.* **765**, L30. DOI. ADS.

Gopalswamy, N., Xie, H., Mäkelä, P., Yashiro, S., Akiyama, S., Uddin, W., Srivastava, A.K., Joshi, N.C., Chandra, R., Manoharan, P.K., et al.: 2013a, Height of shock formation in the solar corona inferred from observations of type II radio bursts and coronal mass ejections. *Adv. Space Res.* **51**, 1981. DOI. ADS.

Grechnev, V.V., Kochanov, A.A., Uralov, A.M.: 2023, Eruptive flare, CME, and shock wave in the 25 August 2001 high-energy solar event. *Solar Phys.* **298**, 49. DOI. ADS.

Grechnev, V.V., Kurt, V.G., Chertok, I.M., Uralov, A.M., Nakajima, H., Altyntsev, A.T., Belov, A.V., Yushkov, B.Y., Kuznetsov, S.N., Kashapova, L.K., Meshalkina, N.S., Prestage, N.P.: 2008, An extreme solar event of 20 January 2005: properties of the flare and the origin of energetic particles. *Solar Phys.* **252**, 149. DOI. ADS.

Grechnev, V.V., Uralov, A.M., Chertok, I.M., Kuzmenko, I.V., Afanasyev, A.N., Meshalkina, N.S., Kalashnikov, S.S., Kubo, Y.: 2011, Coronal shock waves, EUV waves, and their relation to CMEs. I. Reconciliation of "EIT waves", type II radio bursts, and leading edges of CMEs. *Solar Phys.* **273**, 433. DOI. ADS.

Grechnev, V.V., Kiselev, V.I., Uralov, A.M., Meshalkina, N.S., Kochanov, A.A.: 2013a, An updated view of solar eruptive flares and the development of shocks and CMEs: history of the 2006 December 13 GLE-productive extreme event. *Publ. Astron. Soc. Japan* **65**, S9. DOI. ADS.

Grechnev, V.V., Meshalkina, N.S., Chertok, I.M., Kiselev, V.I.: 2013b, Relations between strong high-frequency microwave bursts and proton events. *Publ. Astron. Soc. Japan* **65**, S4. DOI. ADS.

Grechnev, V.V., Kiselev, V.I., Meshalkina, N.S., Chertok, I.M.: 2015, Relations between microwave bursts and near-Earth high-energy proton enhancements and their origin. *Solar Phys.* **290**, 2827. DOI. ADS.

Grechnev, V.V., Uralov, A.M., Kochanov, A.A., Kuzmenko, I.V., Prosovetsky, D.V., Egorov, Y.I., Fainshtein, V.G., Kashapova, L.K.: 2016, A tiny eruptive filament as a flux-rope progenitor and driver of a large-scale CME and wave. *Solar Phys.* **291**, 1173. DOI. ADS.

Grechnev, V.V., Kiselev, V.I., Uralov, A.M., Klein, K.-L., Kochanov, A.A.: 2017b, The 26 December 2001 solar eruptive event responsible for GLE63: III. CME, shock waves, and energetic particles. *Solar Phys.* **292**, 102. DOI. ADS.

Grechnev, V., Uralov, A.M., Kiselev, V.I., Kochanov, A.A.: 2017a, The 26 December 2001 solar eruptive event responsible for GLE63. II. Multi-loop structure of microwave sources in a major long-duration flare. *Solar Phys.* **292**, 3. DOI. ADS.

Grechnev, V.V., Meshalkina, N.S., Uralov, A.M., Kochanov, A.A., Lesovoi, S.V., Myshyakov, I.I., Kiselev, V.I., Zhdanov, D.A., Altyntsev, A.T., Globa, M.V.: 2020, Twin null-point-associated major eruptive three-ribbon flares with unusual microwave spectra. *Solar Phys.* **295**, 128. DOI. ADS.

Grechnev, V.V., Kiselev, V.I., Uralov, A.M., Meshalkina, N.S., Firoz, K.A., Lysenko, A.L.: 2024, Mysteries of the 17 May 2012 solar event responsible for GLE71. I. CME development and the role of disturbances excited by eruptions. *Solar Phys.* **299**, 129. DOI. ADS.

Guidice, D.A.: 1979, Sagamore Hill Radio Observatory, Air Force Geophysics Laboratory, Hanscom Air Force Base, Massachusetts 01731. Report. *Bull. Am. Astron. Soc.* **11**, 311. ADS.

Guidice, D.A., Cliver, E.W., Barron, W.R., Kahler, S.: 1981, The Air Force RSTN system. *Bull. Am. Astron. Soc.* **13**, 553. ADS.

Hanaoka, Y.: 1997, Double-loop configuration of solar flares. *Solar Phys.* **173**, 319. DOI. ADS.

Hannah, I.G., Kontar, E.P.: 2011, The spectral difference between solar flare HXR coronal and footpoint sources due to wave-particle interactions. *Astron. Astrophys.* **529**, A109. DOI. ADS.

Harvey, J.W.: 1969, Magnetic fields associated with solar active-region prominences. PhD thesis, National Solar Observatory, Sunspot New Mexico. ADS.

Hirasima, Y., Okudaira, K., Yamagami, T.: 1970, Solar gamma ray burst observed on 27 Sept. 1968. In: *International Cosmic Ray Conference, Internat. Cosmic Ray Conf.* **2**, 683. ADS.

Hirayama, T.: 1974, Theoretical model of flares and prominences. I: Evaporating flare model. *Solar Phys.* **34**, 323. DOI. ADS.

Hurford, G.J., Schwartz, R.A., Krucker, S., Lin, R.P., Smith, D.M., Vilmer, N.: 2003, First gamma-ray images of a solar flare. *Astrophys. J. Lett.* **595**, L77. DOI. ADS.

Hurford, G.J., Krucker, S., Lin, R.P., Schwartz, R.A., Share, G.H., Smith, D.M.: 2006, Gamma-ray imaging of the 2003 October/November solar flares. *Astrophys. J. Lett.* **644**, L93. DOI. ADS.

Kahler, S.W.: 1982, The role of the big flare syndrome in correlations of solar energetic proton fluxes and associated microwave burst parameters. *J. Geophys. Res.* **87**, 3439. DOI. ADS.

Kiselev, V.I., Meshalkina, N.S., Grechnev, V.V.: 2022, Relationships between the spectra of near-Earth proton enhancements, hard X-ray bursts, and CME speeds. *Solar Phys.* **297**, 53. DOI. ADS.

Klein, K.-L., Trottet, G.: 2001, The origin of solar energetic particle events: coronal acceleration versus shock wave acceleration. *Space Sci. Rev.* **95**, 215. ADS.

Kocharov, L., Pohjolainen, S., Mishev, A., Reiner, M.J., Lee, J., Laitinen, T., Didkovsky, L.V., Pizzo, V.J., Kim, R., Klassen, A., et al.: 2017, Investigating the origins of two extreme solar particle events: proton source profile and associated electromagnetic emissions. *Astrophys. J.* **839**, 79. DOI. ADS.

Kopp, R.A., Pneuman, G.W.: 1976, Magnetic reconnection in the corona and the loop prominence phenomenon. *Solar Phys.* **50**, 85. DOI. ADS.

Krucker, S., Christe, S., Glesener, L., Ishikawa, S.-n., Ramsey, B., Takahashi, T., Watanabe, S., Saito, S., Gubarev, M., Kilaru, K., et al.: 2014, First images from the Focusing Optics X-ray Solar Imager. *Astrophys. J. Lett.* **793**, L32. DOI. ADS.

Kundu, M.R., White, S.M., Gopalswamy, N., Lim, J.: 1994, Millimeter, microwave, hard X-ray, and soft X-ray observations of energetic electron populations in solar flares. *Astrophys. J. Suppl.* **90**, 599. DOI. ADS.

Kundu, M.R., Grechnev, V.V., White, S.M., Schmahl, E.J., Meshalkina, N.S., Kashapova, L.K.: 2009, High-energy emission from a solar flare in hard X-rays and microwaves. *Solar Phys.* **260**, 135. DOI. ADS.

Lee, J., Nita, G.M., Gary, D.E.: 2009, Electron energy and magnetic field derived from solar microwave burst spectra. *Astrophys. J.* **696**, 274. DOI. ADS.

Lemen, J.R., Title, A.M., Akin, D.J., Boerner, P.F., Chou, C., Drake, J.F., Duncan, D.W., Edwards, C.G., Friedlaender, F.M., Heyman, G.F., et al.: 2012, The Atmospheric Imaging Assembly (AIA) on the Solar Dynamics Observatory (SDO). *Solar Phys.* **275**, 17. DOI. ADS.

Lin, R.P., Dennis, B.R., Hurford, G.J., Smith, D.M., Zehnder, A., Harvey, P.R., Curtis, D.W., Pankow, D., Turin, P., Bester, M., et al.: 2002, The Reuven Ramaty High-Energy Solar Spectroscopic Imager (RHESSI). *Solar Phys.* **210**, 3. DOI. ADS.

Longcope, D.W., Beveridge, C.: 2007, A quantitative, topological model of reconnection and flux rope formation in a two-ribbon flare. *Astrophys. J.* **669**, 621. DOI. ADS.

Masson, S., Antiochos, S.K., DeVore, C.R.: 2013, A model for the escape of solar-flare-accelerated particles. *Astrophys. J.* **771**, 82. DOI. ADS.

Masuda, S., Kosugi, T., Hudson, H.S.: 2001, A hard X-ray two-ribbon flare observed with Yohkoh/HXT. *Solar Phys.* **204**, 55. DOI. ADS.

McKenzie, D.E.: 2002, Signatures of reconnection in eruptive flares [invited]. In: Martens, P.C.H., Cauffman, D. (eds.) *Multi-Wavelength Observations of Coronal Structure and Dynamics* **10**, 155. DOI. ADS.

Melnikov, V.F., Magun, A.: 1998, Spectral flattening during solar radio bursts at cm-mm wavelengths and the dynamics of energetic electrons in a flare loop. *Solar Phys.* **178**, 153. DOI. ADS.

Melrose, D.B., Brown, J.C.: 1976, Precipitation in trap models for solar hard X-ray bursts. *Mon. Not. Roy. Astron. Soc.* **176**, 15. DOI. ADS.

Metcalf, T.R., Alexander, D.: 1999, Coronal trapping of energetic flare particles: Yohkoh/HXT observations. *Astrophys. J.* **522**, 1108. DOI. ADS.

Mewaldt, R.A., Looper, M.D., Cohen, C.M.S., Haggerty, D.K., Labrador, A.W., Leske, R.A., Mason, G.M., Mazur, J.E., von Rosenvinge, T.T.: 2012, Energy spectra, composition, and other properties of ground-level events during solar cycle 23. *Space Sci. Rev.* **171**, 97. DOI. ADS.

Miklenic, C.H., Veronig, A.M., Vršnak, B.: 2009, Temporal comparison of nonthermal flare emission and magnetic-flux change rates. *Astron. Astrophys.* **499**, 893. DOI. ADS.

Miroshnichenko, L.I., Vashenyuk, E.V., Pérez-Peraza, J.A.: 2013, Solar cosmic rays: 70 years of ground-based observations. *Geomagn. Aeron.* **53**, 541. DOI. ADS.

Mishev, A.L., Kocharov, L.G., Usoskin, I.G.: 2014, Analysis of the ground level enhancement on 17 May 2012 using data from the global neutron monitor network. *J. Geophys. Res. Space Phys.* **119**, 670. DOI. ADS.

Motorina, G.G., Fleishman, G.D., Kontar, E.P.: 2020, Spatiotemporal energy partitioning in a nonthermally dominated two-loop solar flare. *Astrophys. J.* **890**, 75. DOI. ADS.

Nakajima, H., Sekiguchi, H., Sawa, M., Kai, K., Kawashima, S.: 1985, The radiometer and polarimeters at 80, 35, and 17 GHz for solar observations at Nobeyama. *Publ. Astron. Soc. Japan* **37**, 163. ADS.

Nakajima, H., Nishio, M., Enome, S., Shibasaki, K., Takano, T., Hanaoka, Y., Torii, C., Sekiguchi, H., Bushimata, T., Kawashima, S., Shinohara, N., Irimajiri, Y., Koshiishi, H., Kosugi, T., Shiomi, Y., Sawa, M., Kai, K.: 1994, The Nobeyama radioheliograph. *Proc. IEEE* **82**, 705. ADS.

Nishio, M., Yaji, K., Kosugi, T., Nakajima, H., Sakurai, T.: 1997, Magnetic field configuration in impulsive solar flares inferred from coaligned microwave/X-ray images. *Astrophys. J.* **489**, 976. DOI. ADS.

Nita, G.M., Fleishman, G.D., Kuznetsov, A.A., Anfinogentov, S.A., Stupishin, A.G., Kontar, E.P., Schonfeld, S.J., Klimchuk, J.A., Gary, D.E.: 2023, Data-constrained solar modeling with GX Simulator. *Astrophys. J. Suppl.* **267**, 6. DOI. ADS.

Pal, S., Nandy, D., Srivastava, N., Gopalswamy, N., Panda, S.: 2018, Dependence of coronal mass ejection properties on their solar source active region characteristics and associated flare reconnection flux. *Astrophys. J.* **865**, 4. DOI. ADS.

Papaioannou, A., Sandberg, I., Anastasiadis, A., Kouloumvakos, A., Georgoulis, M.K., Tziotziou, K., Tsiropoula, G., Jiggens, P., Hilgers, A.: 2016, Solar flares, coronal mass ejections and solar energetic particle event characteristics. *J. Space Weather Space Clim.* **6**, A42. DOI. ADS.

Pesnell, W.D., Thompson, B.J., Chamberlin, P.C.: 2012, The Solar Dynamics Observatory (SDO). *Solar Phys.* **275**, 3. DOI. ADS.

Reames, D.V.: 2009, Solar release times of energetic particles in ground-level events. *Astrophys. J.* **693**, 812. DOI. ADS.

Reames, D.V.: 2013, The two sources of solar energetic particles. *Space Sci. Rev.* **175**, 53. DOI. ADS.

Rouillard, A.P., Plotnikov, I., Pinto, R.F., Tirole, M., Lavarra, M., Zucca, P., Vainio, R., Tylka, A.J., Vourlidas, A., De Rosa, M.L., Linker, J., Warmuth, A., Mann, G., Cohen, C.M.S., Mewaldt, R.A.: 2016, Deriving the properties of coronal pressure fronts in 3D: application to the 2012 May 17 ground level enhancement. *Astrophys. J.* **833**, 45. DOI. ADS.

Scherrer, P.H., Schou, J., Bush, R.I., Kosovichev, A.G., Bogart, R.S., Hoeksema, J.T., Liu, Y., Duvall, T.L., Zhao, J., Title, A.M., et al.: 2012, The Helioseismic and Magnetic Imager (HMI) investigation for the Solar Dynamics Observatory (SDO). *Solar Phys.* **275**, 207. DOI. ADS.

Shen, C., Li, G., Kong, X., Hu, J., Sun, X.D., Ding, L., Chen, Y., Wang, Y., Xia, L.: 2013, Compound twin coronal mass ejections in the 2012 May 17 GLE event. *Astrophys. J.* **763**, 114. DOI. ADS.

Silva, A.V.R., Wang, H., Gary, D.E.: 2000, Correlation of microwave and hard X-ray spectral parameters. *Astrophys. J.* **545**, 1116. DOI. ADS.

Simões, P.J.A., Costa, J.E.R.: 2010, Gyrosynchrotron emission from anisotropic pitch-angle distribution of electrons in 3-D solar flare sources. *Solar Phys.* **266**, 109. DOI. ADS.

Sturrock, P.A.: 1966, Model of the high-energy phase of solar flares. *Nature* **211**, 695. DOI. ADS.

Sun, X.: 2013, On the coordinate system of space-weather HMI Active Region Patches (SHARPs): a technical note. arXiv e-prints. arXiv. DOI. ADS.

Tolbert, K., Schwartz, R.: 2020, OSPEX: Object Spectral Executive. ADS.

Torii, C., Tsukiji, Y., Kobayashi, S., Yoshimi, N., Tanaka, H., Enome, S.: 1979, Full-automatic radiopolarimeters for solar patrol at microwave frequencies. *Proc. Res. Inst. Atmos. Nagoya Univ.* **26**, 129. ADS.

Trottet, G., Samwel, S., Klein, K.-L., Dudok de Wit, T., Miteva, R.: 2015, Statistical evidence for contributions of flares and coronal mass ejections to major solar energetic particle events. *Solar Phys.* **290**, 819. DOI. ADS.

Tschernitz, J., Veronig, A.M., Thalmann, J.K., Hinterreiter, J., Pötzi, W.: 2018, Reconnection fluxes in eruptive and confined flares and implications for superflares on the Sun. *Astrophys. J.* **853**, 41. DOI. ADS.

Tylka, A.J., Cohen, C.M.S., Dietrich, W.F., Lee, M.A., Maclennan, C.G., Mewaldt, R.A., Ng, C.K., Reames, D.V.: 2005, Shock geometry, seed populations, and the origin of variable elemental composition at high energies in large gradual solar particle events. *Astrophys. J.* **625**, 474. DOI. ADS.

Tzatzakis, V., Nindos, A., Alissandrakis, C.E.: 2008, A statistical study of microwave flare morphologies. *Solar Phys.* **253**, 79. DOI. ADS.

Veselovsky, I.S., Panasyuk, M.I., Avdyushin, S.I., Bazilevskaya, G.A., Belov, A.V., Bogachev, S.A., Bogod, V.M., Bogomolov, A.V., Bothmer, V., Boyarchuk, K.A., et al.: 2004, Solar and heliospheric phenomena in October–November 2003: causes and effects. *Cosm. Res.* **42**, 435. DOI. ADS.

Vilmer, N., MacKinnon, A.L., Hurford, G.J.: 2011, Properties of energetic ions in the solar atmosphere from γ-ray and neutron observations. *Space Sci. Rev.* **159**, 167. DOI. ADS.

Vršnak, B.: 2016, Solar eruptions: the CME-flare relationship. *Astron. Nachr.* **337**, 1002. DOI. ADS.

White, S.M., Krucker, S., Shibasaki, K., Yokoyama, T., Shimojo, M., Kundu, M.R.: 2003, Radio and hard X-ray images of high-energy electrons in an X-class solar flare. *Astrophys. J. Lett.* **595**, L111. DOI. ADS.

White, S.M., Benz, A.O., Christe, S., Fárník, F., Kundu, M.R., Mann, G., Ning, Z., Raulin, J.-P., Silva-Válio, A.V.R., Saint-Hilaire, P., Vilmer, N., Warmuth, A.: 2011, The relationship between solar radio and hard X-ray emission. *Space Sci. Rev.* **159**, 225. DOI. ADS.

Yashiro, S., Gopalswamy, N., Michalek, G., St. Cyr, O.C., Plunkett, S.P., Rich, N.B., Howard, R.A.: 2004, A catalog of white light coronal mass ejections observed by the SOHO spacecraft. *J. Geophys. Res. Space Phys.* **109**, A07105. DOI. ADS.

Zimovets, I.V., Kuznetsov, S.A., Struminsky, A.B.: 2013, Fine structure of the sources of quasi-periodic pulsations in "single-loop" solar flares. *Astron. Lett.* **39**, 267. DOI. ADS.

Zimovets, I., Vilmer, N., Chian, A.C.-L., Sharykin, I., Struminsky, A.: 2012, Spatially resolved observations of a split-band coronal type II radio burst. *Astron. Astrophys.* **547**, A6. DOI. ADS.

Authors and Affiliations

V.V. Grechnev[1] · V.I. Kiselev[1] · A.M. Uralov[1] · N.S. Meshalkina[1] · A.L. Lysenko[2]

✉ V.V. Grechnev
grechnev@iszf.irk.ru

V.I. Kiselev
valentin_kiselev@iszf.irk.ru

A.M. Uralov
uralov@iszf.irk.ru

N.S. Meshalkina
nata@iszf.irk.ru

A.L. Lysenko
alexandra.lysenko@mail.ioffe.ru

[1] Institute of Solar-Terrestrial Physics SB RAS, Lermontov St. 126A, Irkutsk 664033, Russia

[2] Ioffe Institute, Polytekhnicheskaya 26, St. Petersburg, 194021, Russia